Swift XRT Effective Area measured at the Panter end-to-end tests *

G. Tagliaferri[a], A. Moretti[a], S. Campana[a], A.F. Abbey[c], R.M. Ambrosi[c], L. Angelini[g h], A. Beardmore[c], H. Bräuninger[e], W. Burkert[e], D.N. Burrows[b], M. Capalbi[d], G. Chincarini[a], O. Citterio[a], G. Cusumano[f], M.J. Freyberg[e], P. Giommi[d], G.D. Hartner[e], J.E. Hill[b], K.Mori[b], D. Morris[b], K. Mukerjee[c], J.A. Nousek[b], J. Osborne[c], A.D.T. Short[c], F. Tamburelli[d], D.J. Watson[c], A. Wells[c]

[a] INAF Osservatorio Astronomico di Brera, Italy
[b] Pennsylvania State University, USA
[c] University of Leicester, UK
[d] ASDC, ASI Science Data Center, Frascati, Italy
[e] Max-Planck-Institut für extraterrestrische Physik, Germany
[f] IASF Istituto di Fisica Cosmica ed Applicazioni dell' Informatica, Italy
[g] LHEA, GSFC/NASA
[h] USRA

ABSTRACT

The *Swift* X–ray Telescope (XRT) is designed to make astrometric, spectroscopic and photometric observations of the X–ray emission from Gamma–ray bursts and their afterglows, in the energy band 0.2-10 keV. Here we report first results of the analysis of *Swift* XRT effective area at five different energies as measured during the end-to-end calibration campaign at the Panter X–ray beam line facility. The analysis comprises the study of the effective area both on–axis and off–axis for different event grade selection. We compare the laboratory results with the expectations and show that the measured effective area meets the mission scientific requirements.

Keywords: *Swift*, XRT, Effective Area

1. INTRODUCTION

XRT[1] is a sensitive, autonomous X-ray CCD imaging spectrometer designed to measure the flux, spectrum and light curve of GRBs and afterglow over a wide flux range covering more than seven orders of magnitude. XRT utilizes the third flight mirror module (FM3) developed for the JET–X program[2]: it consists of 12 nested, confocal and coaxial mirror shells having a Wolter I configuration. The mirror diameters range from 191 mm to 300 mm, the nominal focal length is 3500 mm, the total field of view is about 40 arcminutes (at 50% vignetting level at 1.5 keV) and the effective area at 1.5 keV is $\sim$ 165 cm^2. The XRT detector has been designed for the EPIC MOS instruments on XMM–Newton. It is a MAT-22 CCD consisting of 600 x 602 pixels, each 40μm

Copyright 2004 Society of Photo-Optical Instrumentatio Engineers This paper will be published in *Proc. SPIE*, Vol. 5165, and is made available as an electronic preprint with permission of SPIE. One print or electronic copy may be made for personal use only. Systemetic or multiple reproduction, distribution to multiple locations via electronic or other means, duplications of any material in this paper for a fee or for commercial purposes, or modification of the paper are prohibited.

Send correspondence to moretti@merate.mi.astro.it

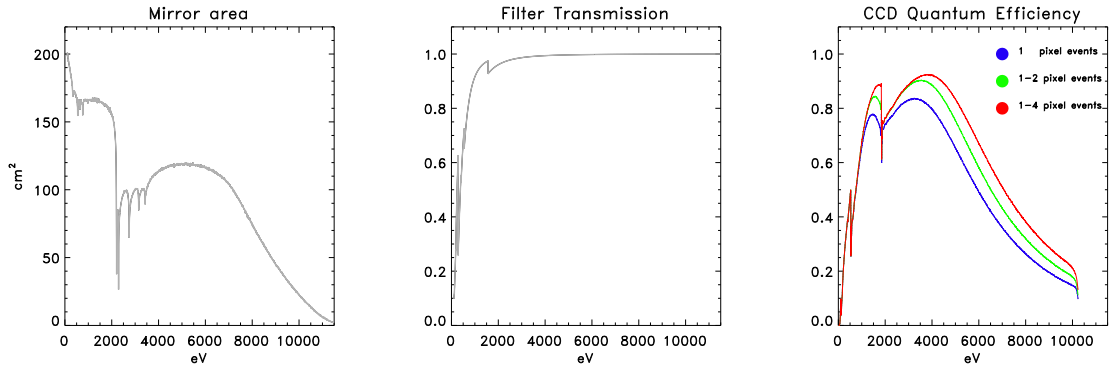

Figure 1. The XRT effective area results from the combination of three factors, here plotted as a function of energy obtained from laboratory tests and software simulations. In the left panel we plot the on–axis mirror area (the mirror area depends on the off–axis). In the central panel the filter transmission curve is plotted. In the right panel the CCD quantum efficiency is plotted for three event grade selections: the dotted line refers to single pixel events, the dashed line to 1-2 pixel events and the continuous line to 1-4 pixel events.

$\times 40\mu$m with a nominal plate scale of 2.36 arcseconds per pixel, which makes the effective field of view of the system $\sim$ 24 arcmin.[1] Moreover a thin filter is required in front of the CCD to block the optical light. Each single component has been deeply tested as a stand-alone unit. The end-to-end calibration campaign of the *Swift* XRT has been carried out in the period September 23rd - October 4th 2002 at the Panter laboratory of the Max-Planck-Institut für extraterrestrische Physik: here we tested the whole integrated system. Monte Carlo simulations and ray tracing software have been developed in order to calculate the effective area of the instrument all over the energy range: the effective area calibration aimed to compare and confirm the expected values at five monochromatic energies.

2. THE MODEL

The effective area is the product of three components: the effective area of the mirror, the quantum efficiency (QE) of the CCD and the filter transmission. To calculate the mirror effective area at different energies a ray–tracing code has been developed at the Osservatorio Astronomico di Brera to evaluate the response of the telescope as part of the JET–X project. This software takes into account the nominal geometry of the telescope and the main physical effects of the focusing process: gold reflectivity and scattering microroughness.[3] The effective area depends on the distance from the optical axis (i.e. the off–axis angle), the so called vignetting factor. CCD QE measurements have been made at the University of Leicester and at the Orsay sychrotron. These measurements have been incorporated into Monte Carlo and an analytical model developed to simulate QE and spectral response of the CCDs of the *Swift* XRT.[4] In general the charge produced in the CCD by an X–ray event occupies more than one pixel and less than nine pixels. The QE is calculated as a function of the number of pixels occupied by the X–ray events (ranging from 1 to 9). The filter transmission as a function of energy has been created from the manufacturer-supplied composition data (1840 Angstroms polyimide + 488 Angstroms Aluminium). To confirm these values, measurements have been taken at Leicester using the EPIC X-ray test facility (using a SiLi detector) at 10 different energies: these measurements are fully consistent with this filter transmission curve.[4] The three unit responses as function of energy are plotted in Fig 1. The

effective area of the XRT telescope is the product of these three units: the main goal of the effective area end-to-end calibration is to compare the response of the integrated system with the expectations derived from the calibration of the three single units.

3. THE DATA

Calibration data have been collected at five energies (Tab.1) in all the four operational modes of the XRT telescope[5] both on–axis and at four off–axis angles in two perpendicular directions (Fig.2). In particular

Table 1. The values of the 5 calibration energies used for effective area calibration.

Source	C-K	Al-K	Ti-K	Fe-K	Cu-K
Energy [keV]	0.28	1.49	4.51	6.40	8.05

Windowed Timing (WT), Photo Diode (PD) and Photon Counting (PC) data have been collected only on–axis and provide the absolute calibration of the effective area, whereas Imaging Mode (IM) data have been collected both on– and off–axis, and provide the relative calibration. The timing modes (PD and WT) allow to observe high flux sources, whereas PC mode is suited for very low fluxes ($\leq$ 1 count sec^{-1}). Therefore, due to the short time available for the end-to-end effective area calibration, the most reliable observations have been performed in timing modes where the necessary statistics could be reached in short exposure ($\leq$ 100 sec). For each energy we have also one long exposure ($\sim$ 5000 sec) performed in PC mode but they are affected by large statistical uncertainties (see below). We first measure the absolute value of the effective area on–axis, by means of the timing modes data and then we determined the vignetting factor from the comparison between on– and off–axis imaging data.

At the Panter X–ray beam line facility the source has been positioned at 130 meters from the XRT mirror. The input flux is calibrated by means of a proportional counter near the instrument. Given $influx$ as the input count–rate cm^{-2} in a given narrow energy band (as measured by the proportionl counter near the mirror) and *outrate* as the count–rate measured by the XRT focal plane camera, we obtain a first measurement of the effective area of our instrument $A_{@130}$ from the simple formula:

$$A_{@130}[cm^2] = \frac{outrate[sec^{-1}]}{influx[sec^{-1}cm^{-2}]}.$$

To get the real value of the telescope effective area A_∞ for a source at an infinite distance, we have to correct for the divergence of the Panter Facility X–ray beam, which causes a loss of area due to the the lack of secondary reflection of some photons. This loss has been estimated by means of the ray tracing software: it depends on the energy and ranges from $\sim$ 4% at the C-K energy (0.3 keV) to $\sim$ 20% in the case of Cu-K (8.0 keV). We have also to apply the PSF correction, which is different for the four different modes. In PC mode we counted the total counts within a circle of 40 pixel radius: this implies a loss of photons of $\sim$ 5% for the highest energies. In PD mode we are forced to collect photons from all the detector (including the corner sources, see below) and this makes the PSF correction negligible. More important is the PSF correction in WT mode where the on–axis position is at 30 pixels from the border of the window: this produces at the highest energy a correction of $\sim$ 10%.

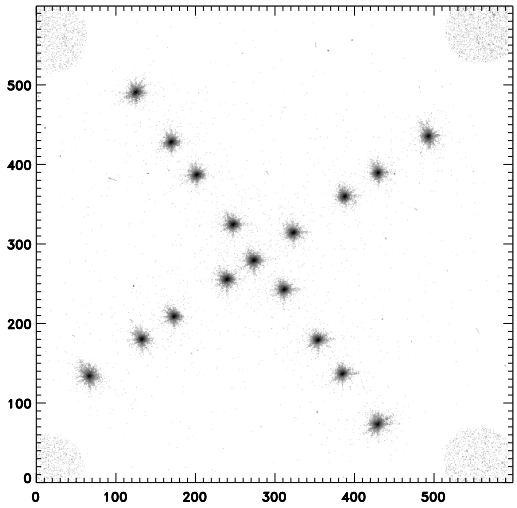

Figure 2. This figure shows the different positions used to study the effective area dependence on the off–axis angle in the case of the Al-K: the figure is produced by summing up different images taken at different times.

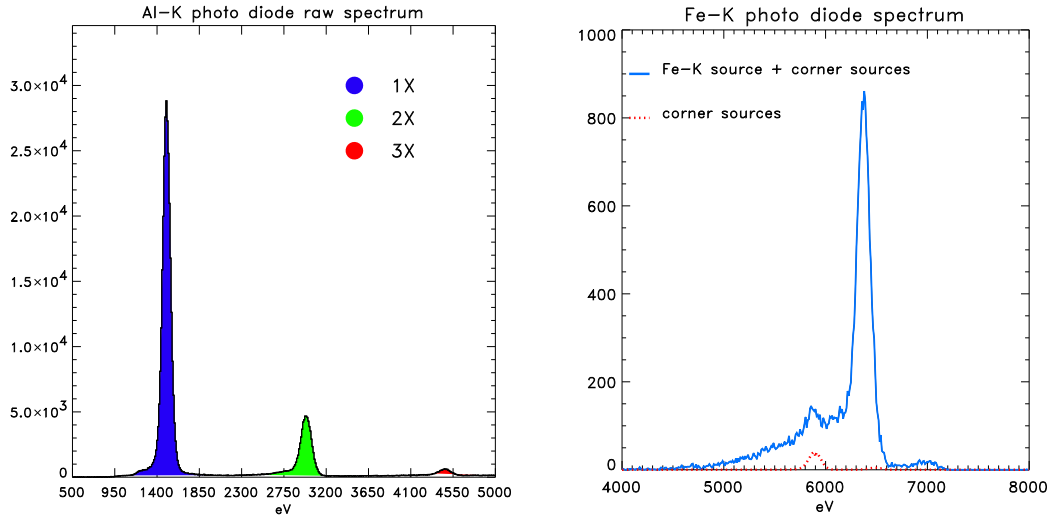

Figure 3. The left panel illustrates how we counted the X–ray events in a generic piled up spectrum: we weighted the events of the second and third piled up peaks by a factor of two and three respectively. In the right panel we plot a PD mode Fe-K spectrum (the grey line) which includes the contamination due to the corner source fluxes. A corner source spectrum (black dashed line) as observed in PC mode is also shown. The exposure is $\sim$ 84 seconds with a count rate of $\sim$ 250 counts sec^{-1} and in this case we estimate that the contamination from the corner source is $\sim$ 3%.

Because of the pile up effect a fraction of events originally belonging to the energy band E is added up and registered as events with energy 2×E or n×E. To take this effect properly into account we calculate the total counts at the CCD using the formula:

$$totalcounts = N_E + 2 \times N_{2E} + ... + n \times N_{nE}$$

where N_nE is the number of events recorded within the energy band [n-1E, nE] as illustrated in Fig. 3.

In PD mode we have to take into account the presence of the four Fe55 calibration sources at the corners of the detector that produce a Mn-K alpha and beta line at 5.9 and 6.5 keV. We extract their spectra from the longest PC mode exposures and we subtract their contribution from PD mode observations. At lower energies the contribution is completely negligible, but in the cases of Fe-K they contribute with ~ 8 counts sec^{-1} (Fig. 3).

4. THE ON–AXIS MEASUREMENTS

In the context of the calibration of the effective area the main difference among the four operational modes are the procedures used to reconstruct the X–ray events. The charge produced in the CCD by an X–ray event is splitted over a number of adiacent pixels within a box of 3×3. X–ray events have particular shapes (single pixel, vertically and horizontally 2 pixels, L-shaped, etc.) which distinguish them from the charge produced by cosmic rays which have usually more complicated shapes.

In WT mode the spatial information is 1-dimensional and the 3×3 box around an X–ray event is accumulated in a 3×1 box. This prevents the possibility of reconstructing the events according to their original shapes and prevents a perfect selection of real events from cosmic rays. In the 3×1 box an event can be classified as single, 2 or 3 pixel event. WT 1 pixel events are made up by intrinsic 1-pixel and some 2-pixel events. WT 2 pixel events are made up of intrinsically 2, 3, 4 and 5–pixel events: in this case some cosmic rays could be considered as real X–ray events producing some contamination.

Analogously, in PD mode the 3×3 box is accumulated on a 5×1 box and the events are classified as single, 2, 3, 4, 5 pixel events. PD 1 pixel events are mostly intrinsic isolated pixels; PD 2 pixel events are made up of intrinsic 2 and some 3 pixel events; PD 3 pixel events are made up of intrinsic 3, 4 and some 5 pixel events: in this case some cosmic rays could be considered as real X–ray event producing some contamination. PD 4 and 5 pixel events are intrinsically 5-9 pixel events, but are highly contaminated by cosmic rays.

In PC mode a full 3×3 pixels reconstruction is possible and the ground reduction software provide an ASCA grade for each event. ASCA grade 0 corresponds to single pixel events; ASCA grades 0, 2, 3, 4 correspond to 1-2 pixels events and ASCA grades 0, 2, 3, 4, 6 to 1-4 pixels events. We summarize this scheme in Tab. 2.

In Imaging mode (suited to determine only the position of the GRB and to provide a coarse estimate of the flux) the charge produced by an X–ray event is read directly, without the event reconstruction, consequently most of the energy information is lost.

In Fig. 4 we compare the results from WT mode observations with the model. The plotted values are the mean of various measurements (typically five) taken with different source count rates and the errors are the standard deviations. As already explained in WT mode some intrinsic two pixel events are considered as single pixel events: in the left panel we compare the results derived for single pixel WT mode data with the expectation for one and two pixel event effective area. In the right panel we compare the results derived for the two pixel WT mode data with the four pixel model (see Tab. 2) finding a good agreement.

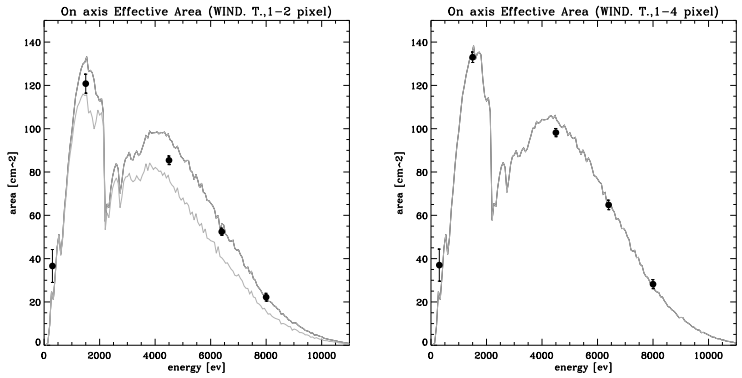

Figure 4. In WT mode some intrinsic two pixel events are considered as single pixel events: in the left panel we compare the results derived for single pixel WT mode data with the expectation for one and two pixel event effective area. In the right panel we compare the two pixel WT mode data with the four pixel model (see Tab. 2) finding good agreement. The plotted values are the mean of different measurements (typically five) taken with different source count rates and the errors are the standard deviations.

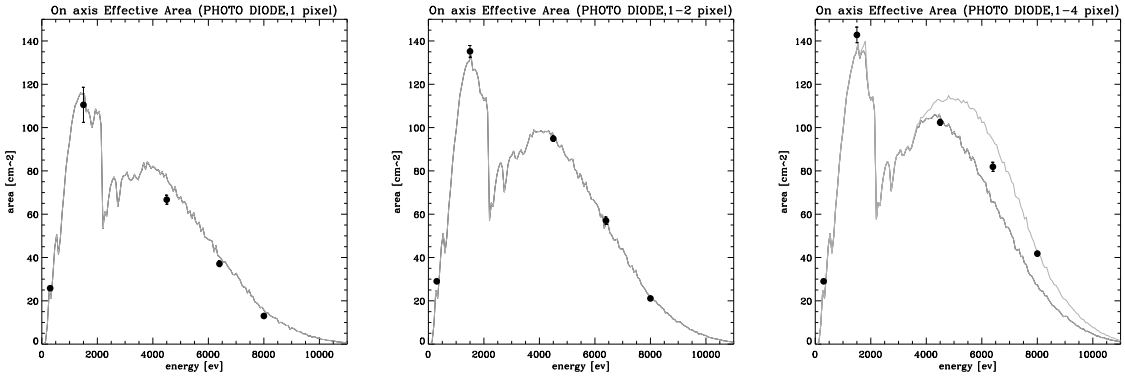

Figure 5. The results of the PD mode measurements. We find a good agreement between the observations and the model in the case of 1 and 2 pixel events. For three pixel PD events, at high energies, we find values higher than the expectations, probably due to a significant level of contamination either from cosmic rays and/or from 5-9 pixel X–ray events. In this panel data are compared with the effective area expected for 4-pixel and 9 pixel event. The plotted values are the mean of different measurements (typically five) taken with different source count rates and the errors are the standard deviations.

In Fig. 5 we plot the measurements of the effective area at the five monochromatic energies observed in PD mode compared with the expected values. Note the good agreement between observations and the model. On the contrary in the case of three pixel PD events there seems to be a significant level of contamination either from cosmic rays and/or from 5-9 pixel X–ray events.

In Fig. 6 we report the results of the low rate PC mode observations. In this case we have only one measurement at each energy and the errors are the statistical uncertainties present both in the measured and

Table 2. The expected effective area depends on the grade selection. Each operational mode allows different ways of reconstructing the events and correspondingly different grade classification. In this table for three different types of event (1 pixel, 1-2 pixel, 1-4 pixel) we report the corresponding grades in the different operational modes. This is the basis to derive the results from different operational modes.

intrinsic pixels	PC[ASCA GRADES]	WT[pixels]	PD[pixels]
1	0	–	1
1-2	0, 2, 3, 4	1	1, 2
1-4	0, 2, 3, 4, 6	1, 2	1, 2, 3

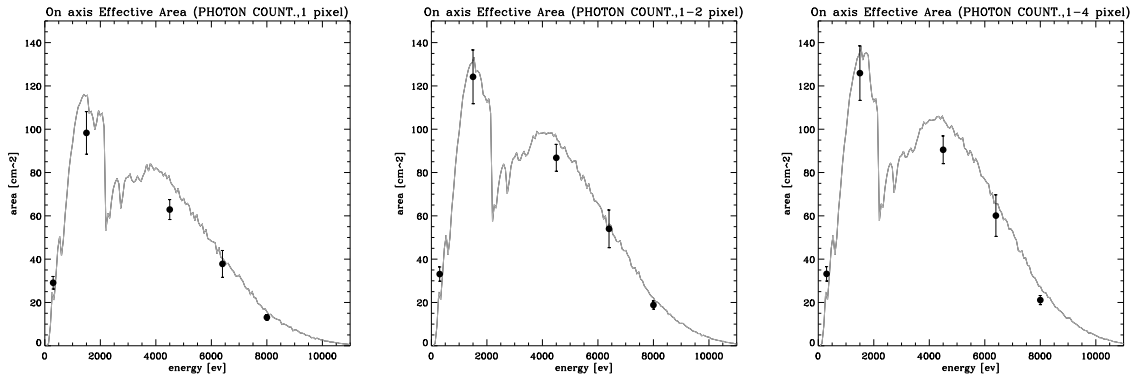

Figure 6. Here we compare ASCA grade selection data (see Tab. 2) with the expected area. The left panel shows ASCA grade 0 with the expected area for 1 pixel event, the central panel shows ASCA grades 0,2,3,4 with the expected area for 1-2 pixels events and the right panel shows ASCA grades 0,2,3,4,6 with the expected area for 1-4 pixels events.

in the input count rate. The main source of uncertainty in this case is the input flux measurements from the proportional counter due to the low statistics. Although the uncertainties are large the PC mode effective area measurements seem to be systematically lower by 5-10% than the expected values. The typical count rates of these observations are 0.5-1 count sec^{-1} (2-3 counts per frame) which could produce some pile up and consequently a grade migration effect. This could affect the effective area measurements.

In the near future some improvements of our work will come from the implementation of the XMM EPIC–MOS grade classification in the XRT data analysis software. This will allow us a more flexible grade classification and a more precise estimate of the cosmic ray contamination in the timing modes. The mission requirements for the effective area were 100 cm^2 at the Al-K energy (1.5 keV) and 15 cm^2 at the Cu-K energy (8.0 keV). These values have to be compared with the area relative to 1-4 pixel events. Thus, our results show that the XRT requirements are fully met and that its final effective area is in line with the expectations.

5. THE OFF–AXIS MEASUREMENTS: THE VIGNETTING

For an X–ray source which is not on the optical axis of the telescope both the reflection efficiency and the geometric collecting area of the telescope are lower as a function of the off–axis angle. Moreover, this effect depends on the energy. In Fig. 7 we plot the relative effective area measurements as function of the off–axis

Table 3. Summary of the measurements (cm^2). In parenthesis we report the expected values. The errors are the standard deviation of the measurements (typically we have five measurements for each energy and for each operational mode). In the case of the PC mode we have only one measurement for each energy and the quoted errors are the statistical errors for the single measurement.

	C–K	Al–K	Ti–K	Fe–K	Cu–K
WT 1-2	36.6±7.6 (31.2)	120.8±4.4 (131.4)	85.4±2.0 (95.9)	52.4±1.7 (56.0)	22.2±1.8 (20.9)
WT 1-4	37.0±7.4 (31.2)	133.0±2.4 (135.4)	98.2±1.9 (104.6)	64.8±2.2 (65.6)	28.2±2.1 (26.0)
PD 1	25.8±0.5 (31.1)	110.5±8.1 (115.4)	66.7±2.1 (76.5)	37.1±1.3 (40.3)	13.0±0.3 (14.8)
PD 1-2	29.0±0.9 (31.2)	135.2±2.7 (131.4)	94.9±1.2 (95.9)	57.0±1.7 (56.0)	21.1±0.9 (20.9)
PD 1-4	29.0±0.9 (31.2)	142.8±3.6 (135.4)	102.4±1.4 (104.6)	81.9±2.1 (65.6)	41.8±1.0 (26.0)
PC 1	29.1±2.9 (31.1)	98.3±9.8 (115.4)	62.9±4.6 (76.5)	37.8±6.2 (40.3)	13.1±1.3 (14.8)
PC 1-2	33.1±3.3 (31.2)	124.2±12.4 (131.4)	86.8±6.2 (95.9)	54.0±8.7 (56.0)	18.8±1.8 (20.9)
PC 1-4	33.2±3.3 (31.2)	125.9±12.5 (135.4)	90.5±6.4 (104.6)	60.1±9.6 (65.6)	21.1±2.1 (26.0)

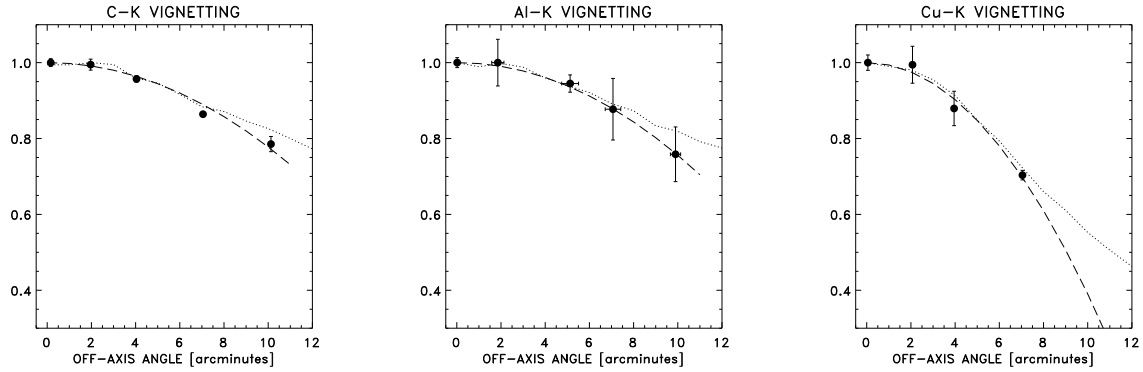

Figure 7. The vignetting effect at three different energies. The data (black dots) are fitted with a function $1\text{-}cx^2$ (dashed lines). The data are also compared with the results of the ray tracing simulations (dotted line) finding a very good agreement up to 8 arcminutes of off–axis angle.

angle for three energies. It is evident that at a given off–axis angle the vignetting effect is larger at higher energies. In order to be able to calculate the vignetting correction for a generic spectrum in any position of the detector we use the following procedure. For each calibration monochromatic energy we fit the vignetting correction as a function of the off–axis angle θ with the function $1\text{-}c\theta^2$ where c is function of energy E: c=c(E). This function provides a good fit to the data (see Fig. 7). Note also the perfect agreement of the measurement with the ray tracing simulations. Then, we fit the five values of the coefficient c(E) with an exponential factor as illustrated in Fig. 8 and we obtain the $\mathrm{Vig}(E,\theta)=1\text{-}c(E)\theta^2$. Again we are obtaining a good fit, thus with this analytical parametrization we can easily apply the vignetting correction at any given position and at any energy. This is in line with what we did for the PSF correction[6] .

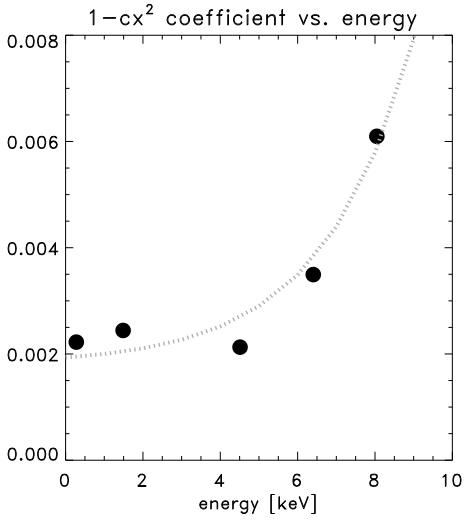

Figure 8. The vignetting effect has a clear dependence on the energy: at a given off–axis angle the effect is larger at higher energies. We parametrize this dependence by means of the coefficient c of the 1-cx^2 function (the filled circles in the plot) which can be well fitted by an exponential function (dotted line).

6. CONCLUSIONS

The effective area end–to–end calibration demonstrated that XRT meets the mission requirements in terms of effective area. Some improvements of our work will come in the near future from the implementations of the new software for the event reconstruction based on the XMM EPIC–MOS classification scheme.

REFERENCES

1. D. Burrows, J. Hill, J. Nousek, A. Wells, G. Chincarini, A. Moretti, S. Campana, A. Abbey, A. Beardmore, J. Bosworth, H. Braeuninger, W. Burkert, M. Capalbi, W. Chang, O. Citterio, M. Freyberg, P. Giommi, G. Hartner, R. Killough, B. Kittle, R.Klar, C. Mangels, M. McMeekin, B. Miles, A. Moretti, K.Mori, D. Morris, K. Mukerjee, J. Osborne, A. Short, G. Tagliaferri, F. Tamburelli, D. Watson, R. Willingale, and M. Zugger, "The swift x–ray telescope," *Proc. SPIE* **5165**, p. these proceedings, 2003.
2. O. Citterio, S. Campana, P. Conconi, M.Ghigo, F. Mazzoleni, E. Poretti, G. Conti, G. Cusumano, B.Sacco, H. Braeuninger, W.Burkert, R. Egger, C. Castelli, and R. Willingale, "Characteristics of the flight model optics for the jet-x telescope onboard the spectrum x-γ satellite," *Proc. SPIE* **2805**, p. 56, 1996.
3. O. Citterio, P. Conconi, M.Ghigo, R. Loi, F. Mazzoleni, E. Poretti, G. Conti, T. Mineo, B.Sacco, H. Braeuninger, and W.Burkert, "X-ray optics for the jet-x experiment aboard the spectrum-x satellite," *Proc. SPIE* **2279**, p. 480, 1994.
4. K. Mukerjee, J. P. Osborne, A. Wells, A. F. Abbey, A. P. Beadmore, A. D. Short, R. M. Ambrosi, and A. Moretti, "The spectroscopic performamce of the swift x-ray telescope for gamma ray bursts afterglows study," *Proc. SPIE* **5165**, p. these proceedings, 2003.

5. J. Hill, D. Burrows, J. Hill, J. Nousek, , A. Abbey, R. Ambrosi, H. Braeuninger, W. Burkert, M. Capalbi, C. Cheruvu, G. Cusumano, M. Freyberg, G. Hartner, R. Klar, A. Moretti, K.Mori, D. Morris, A. Short, G. T. D. Watson, P. Wood, and A. Wells, "Readout modes and automated operations of the swift x–ray telescope," *Proc. SPIE* **5165**, p. these proceedings, 2003.
6. A. Moretti, G. Tagliaferri, A. Moretti, S. Campana, A. Abbey, R. Ambrosi, L. Angelini, A. Beardmore, H. Braeuninger, W. Burkert, D. Burrows, M. Capalbi, G. Chincarini, O. Citterio, G. Cusumano, M. Freyberg, P. Giommi, G. Hartner, J. Hill, K.Mori, D. Morris, K. Mukerjee, J. Nousek, J. Osborne, A. Short, F. Tamburelli, D. Watson, and A. Wells, "Swift xrt point spread function measured at the panter end–to–end tests," *Proc. SPIE* **5165**, p. these proceedings, 2003.